Electronic effects due to organic linker-metal surface interactions: implications on screening of MOF-encapsulated catalysts

Benjamin Schweitzer,[a] ǂ Chloe Archuleta,[a] ǂ Bomsaerah Seong,[a] Ryther Anderson, [a] Diego A. Gómez-Gualdrón[a] *

[a] Department of Chemical and Biological Engineering, Colorado School of Mines, Golden CO 80401, USA

ABSTRACT: MOF-encapsulated nanoparticles (NP@MOFs) are hybrid, heterogeneous catalysts, where the MOF could boost the activity and selectivity of the encapsulated NP for the reaction of choice by controlling reactant orientation. However, due to overwhelming combinatorics, methods to rapidly identify promising NP + MOF combinations for a given application are needed. Earlier work used a "surrogate" inert pore on top of NP-representative surfaces to generically capture MOF steric effects, hence enabling computational screening to focus on NP composition. However, the surrogate pore method neglects electronic effects of the MOF on the NP. Here, we use density functional theory to study how paradigmatic MOF linkers (imidazolate, carboxylate, and thiolate) impact the electronic structure of representative metal surfaces, and in turn the binding of small species, whose formation energies are commonly used in descriptor-based catalyst screening. We find that the coordinating moiety and functionalization of the linker modulates the shift in the metal d-band center and the electron transfer, which is correlated to experimentally measurable quantities such as C-O vibration frequencies. However, in the majority of cases, the effect of the linker on binding energies (for C*, O*, N*, H*, OH*, CH_3* and CO*) was less than 10 kJ/mol. Furthermore, scaling relationships between binding energies were only slightly affected by linker-originated electronic effects. Therefore, activity/selectivity "heat maps" derived from calculations under "generic" steric constrains could remain useful to screen the optimal NP composition of an NP@MOF catalyst. On the other hand, the placement of a given NP composition on the aforementioned heat maps is affected by the MOF. For an n-butane oxidation case study, we estimated that Ag_3Pd—a promising NP composition for selective 1-butanol formation according to previous screenings using the surrogate pore method—has a ~85% probability of retaining a selectivity for 1-butanol above 75% when encapsulated in carboxylic MOF of suitable pore size.

■ INTRODUCTION

The chemical industry, which is primarily based on heterogeneous catalysts, accounts for ~50% of U.S. energy expenditures in the industrial sector, which itself accounts for ~20% of all energy consumption.[1] This is partly due to the need for *i)* energy-intensive separation processes to isolate desired products,[2] which stems from non-selective reactions, *ii)* high energy input to reactors, which stems from requiring high temperature to activate reactants. Indeed, activating reactants at mild conditions and achieving high selectivities are grand challenges in catalysis,[3] and ones that need to be met if large-scale chemical processes are to be made more energy-efficient. Enzymatic catalysts offer high selectivity and activity at mild conditions,[4,5] but are not as easy to recover and as amenable to scale-up as heterogenous catalysts. Therefore, an ambitious goal is to impart heterogenous catalysts with selectivities and activities similar to enzymes. This may be done by introducing atomistic features found in enzymes into the heterogenous catalyst design.

Enzymes, which present a catalytic center embedded into an organic "shell," are selective and active primarily because the shell sterically controls the orientation of reactants as they reach the active site and stabilizes the relevant transition state.[6] Therefore, one way to impart similar features in heterogenous systems is by encapsulating catalytically nanoparticles (NPs). In a prominent effort, Medlin and coworkers[7] showed that by enshrouding Pd NPs with thiolates, the selectivity of furfural reactions was altered. This approach continues to be explored experimentally[8-12] and computationally,[13,14] but potential drawbacks are that only a few active sites are exposed and deliberate control of reactant orientation is rather difficult.[15]

In recent years, an approach that has been gaining momentum is the encapsulation of NPs in porous crystals (NP@PC) such as metal-organic frameworks (MOFs).[16-21] This approach has shown potential for selectivity control. For instance, Farha and coworkers[17] showed that Pt@ZIF-8 regioselectively hydrogenates 1,3-hexadiene, while Yaghi and coworkers[22,23] showed that Pt@Zr-MOF hydrogenative conversion of methylcyclopentane to different products depending on the type of Zr-MOF encapsulating the catalyst. There is also evidence that encapsulation can facilitate activation at lower temperature. For instance, Zhu and coworkers[24] calculated smaller barriers for CO oxidation on Au_{16} than on Au_{16}@ZIF-8.

Based on the above, tuning the NP and MOF composition in NP@MOFs is a promising way to achieve high selectivity and activity under mild conditions in heterogenous systems. However, due to exploding combinatorics, the chal-

lenge is to find the optimal coupling of NP and MOF compositions for a reaction of interest. Consider that (i) only considering binary alloys in three stoichiometries, Greeley and coworkers[25] studied 786 alloys, (ii) only considering non-functionalized crystals, Gómez-Gualdrón and coworkers[26] studied 13,512 MOFs. Therefore, if one were to combine these MOFs and alloys, one would already be looking into 10,620,432 potential NP@MOFs. Considering the significant effort involved in synthetically realizing each new NP@MOF (as reflected in the relatively few NP@MOF variations experimentally tested so far), strategies for computational high throughput screening akin to those established for traditional catalysts[27] are required to accelerate the development of this emergent type of catalyst.

Gómez-Gualdrón and coworkers[28] proposed that by assuming that the "MOF effect" is mostly the imposition of steric constraints, it was possible to explore NP compositions for the reaction of interest via density functional theory (DFT) by using a generic "surrogate pore" (made of inert He atoms) to provide those constraints. Getman and coworkers[29] used this approach to elucidate relevant reaction pathways for oxidation of n-butane on Ag_3Pd under generic steric constraints. Moreover, combining this approach with degrees of rate control, Campbell and coworkers[30] found that the use of H_2O as oxidant would be crucial to enable the selective oxidation of n-butane to 1-butanol on Ag_3Pd. Most recently, Zhu and Getman[31] explored more NP compositions under steric constraints (Pd, PdZn, Ag_3Pd, Cu_3Pd, and Cu) for the above reaction. Note that the rational for the above studies was that the steric constraints in a suitable NP@MOF would prevent the oxidation of the secondary carbon. Thus, the remaining issue was to tune the NP composition to be active enough to activate the primary carbon, but not enough as to overdehydrogenate it.

On the other hand, since the surrogate pore does not interact with the NP surface as the MOF does, there is some uncertainty whether a "promising" NP composition identified in screenings with the surrogate pore would still be promising under constraints by an actual MOF. Thus, it is important to understand how interactions between MOF and NP affect the electronic structure of the NP and, in turn, the reaction energetics (and ultimately, the conclusion that an encapsulated NP composition is optimal). Some initial forays in this area were made by Huang and coworkers,[32] who synthesized Pd@UiO-66-X systems via the so-called "ship-in-a-bottle"[33] approach. These authors used DFT to study the interaction of Pd_{38} clusters with the functional groups of C_6H_6, C_5H_6-OCH_3 and C_6H_5-NH_2, hence representing the interaction of linkers with metallic clusters grown within the well-defined characteristic cavities of the host MOF. These authors calculated the charge transferred to Pd_{38} from amino and ester linker functional groups, which they linked to the experimentally observed enhancement or hindering of the oxidation capability of Pd due to encapsulation in UiO-66-X.

Similar studies on electronic effects for NP@MOFs synthesized via the "bottle-around-ship"[33] method are yet to be done. Perhaps, an obstacle for these studies has been the unknown atomistic details of the NP/MOF interface in these systems, where the encapsulated NPs are known to be larger than the characteristic cavities of the host MOF. Recently, however, Stair and coworkers[34] combined DRIFTS and NMR experiments with DFT calculations to conceive an atomistically detailed interface model (**Fig. 1)** for Pt@ZIF-8, where Pt NPs (d=~5 nm) are encapsulated by ZIF-8 (characteristic pore size = 1.1 nm). A key feature of the interface model is that MOF linkers bind to the NP surface through the same chemical moiety that they use to coordinate with MOF inorganic nodes. This new understanding provides an opportunity to interrogate to what extent electronic effects originating from linker-NP interactions affect catalytic activity and/or selectivity.

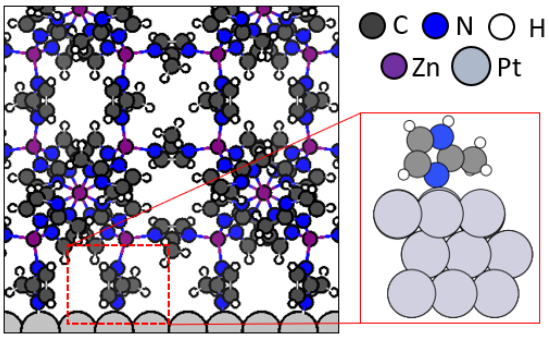

Figure 1. Atomistically-detailed interface model for Pt@ZIF-8 conceived from experiments and DFT calculations in ref. [34], and their simplified slab model to interrogate vibrational shifts on chemisorbed CO.

In this work, we use DFT calculations to explore to what extent the electronic structure of various closed-packed catalytic surfaces (representing the surface of encapsulated NP) is altered by its interaction with organic linkers (which represent the MOF). First, we calculate binding energies of MOF coordinating moieties on Au, Cu, Pt, Pd and Ni to support the proposition that NP/MOF interface structures analogous to **Fig. 1** are also plausible in other NP@MOFs besides Pt@ZIF-8. Then, we determine the electronic effects of linker binding and how these in turn affect the binding of common small chemical species such as H*, N*, O*, OH*, CH_3*, C*, and CO*. These species were chosen because they often appear in well-known scaling relationships that relate binding energies of these species to activation energies (which are necessary to develop microkinetic models). We perform a somewhat more detailed analysis on the binding of CO, due to the potential of CO-sorption DRIFTs experiments to help characterize NP@MOF systems. Then, we examine how the linker coordination-induced variations in C* and OH* binding energies would alter the positioning of screened metals on 2D-volcano plots for catalyst activity and selectivity for n-butane oxidation to 1-butanol under steric constraints. For examining the latter case study, we exploit the microkinetic model developed by Zhu and Getman.[31]

■ COMPUTATIONAL METHODS

Plane-wave density functional theory (PW-DFT) calculations were performed using the VASP.5.3.1 ab-initio code.[35-37] Consistent with relevant preceding work,[28-31] our calculations use the GGA Purdue-Burke-Ernzerhof (PBE) functional[38] to model the electron exchange and correlation, along with the D2 corrections by Grimme[39] to explicitly model dispersion interactions. An energy cutoff of 500 eV

was used to define the Block wave basis set to construct the solutions to the Kohn-Sham equations. All simulations used spin polarization. Gaussian smearing[40] was used to accelerate energy convergence with respect to number of k-points, with a smearing parameter of 0.03, which kept T*S under 1 x 10^{-3} eV. Electronic and atomic configurations were considered converged when energy and forces fell below 10^{-5} eV and 10^{-2} eV/Å, respectively.

Preceding slab calculations, bulk unit cells were optimized to obtain lattice constants. These optimizations used 9 x 9 x 9 Gamma-centered k-point meshes for cubic cells, or equivalently spaced meshes for non-cubic ones. Calculated lattice constants were within the expected accuracy for the PBE functional (~2 %). The slabs for slab calculations were obtained by cleaving the optimized bulk unit cell to expose the most closed-packed surface, which was done using the Crystal Builder module in Materials Studio.[41] The same module was used to place MOF linkers and adsorbates on the slab surface. Slabs were at least 3-layered with at least 1 layer frozen, leaving a 30 Å vacuum space between the slabs in the direction perpendicular to the surface. This enabled more than 20 Å between surface-bound linkers and slab periodic images, which has been suggested to be sufficient to converge results with respect to slab separation.[42] On the other hand, while a higher number of layers would be needed to fully converge adsorbate binding energies, here we are focused on how these energies (and the metal slab electronic structure) are altered by linker-metal interactions. A 4 x 4 x 1 k-point mesh was used for slab calculations, as further increasing the mesh density was found to not significantly alter binding energies. All binding energies were calculated as the energy released when the slab without the adsorbate and the isolate adsorbate are brought together.

Electron densities in optimized slab configurations were obtained using an 8 x 8 x 1 k-point mesh and the tetrahedron smearing method with Blochl corrections. From these densities, atomic charges were obtained using the Bader splitting formalism.[43,44] To calculate the electronic density of states (DOS), the obtained electron density was used in a nonselfconsistent calculation. The d-band center was calculated as the first moment of the DOS projected on d-states of the surface atoms. Consistent with earlier work,[34] adsorbate vibrations were decoupled from the surfaces, so adsorbate vibration frequencies were calculated while keeping all non-adsorbate atoms frozen. Vibrations were obtained by the "finite-displacement" method by systematically displacing adsorbate atoms 0.05 Å in all directions. Calculations on isolated species were done at the gamma-point on a 15 Å x 15 Å x 20 Å orthorhombic cell.

The microkinetic model for the oxidation of n-butanol was built using the scaling relationships developed by Zhu and Getman in ref. [31], which are based on formation (electronic) energies without zero-point energy (ZPE) corrections. The microkinetic model was constructed using the CatMap software developed by Medford and coworkers.[45]

■ RESULTS AND DISCUSSION

Organic linker binding. Following the findings by Stair and coworkers,[34] we postulate that the "bottle-around-ship" NP@MOF synthesis method results in similar NP/MOF interfaces where MOF linkers bind the NP surface as N-methylimidazolate binds Pt in **Fig. 1**. Thus, to investigate the extent of electronic effects by other MOFs on other NPs, we considered the analogous binding of other linker coordinating moieties to other metals. Acrylate was used to represent the coordinating moiety of common carboxylate (**C**) MOFs. The vinyl moiety was intended to provide a similar π electron cloud near the α-carbon as to mimic the behavior of the carboxylate moiety in common phenyl-based carboxylate MOF linkers, but at lower computational cost. Comparing the distribution of charges and the lowest-unoccupied molecular orbital (LUMO) between benzene dicarboxylate and acrylate suggests this to be the case (**Fig. S1**). The LUMO is relevant because the carboxylate moiety withdraws electrons from the metal surface (*vide infra*), which are received by this orbital. Imidazole was used to directly represent the coordinating moiety pertinent to imidazolate (**I**) MOFs (i.e. zeolitic imidazolate frameworks; ZIFs). Ethanethiolate was added as a reference representing the thiolate coordinating moiety (**T**) pertinent to typical NP-enshrouding self-assembled monolayers.[7] However, it may also be pertinent to NP encapsulation in some MOFs based on sulfur-metal coordination, such as those explored for high electrical conductivity.[46,47]

The "surface coverage" by organic linkers in our calculations (one linker in a 3 x 3 supercell) is consistent with the coverage of methyl imidazole on Pt in Pt@ZIF-8, which was estimated from CO sorption experiments and modeling.[34] **Fig. 2** illustrates the optimized binding configurations for imidazole, acrylate and ethanethiolate on Pt(111). No constraints were used during optimization of imidazole and acrylate binding but, in the ethanethiolate case, the S-C bond was constrained to remain perpendicular to the metal surface. The most stable linker binding configurations were explored in Pt(111) and assumed to hold for other studied surfaces. Therefore, analogous binding configurations to those in **Fig. 2** were obtained for the Au(111), Cu(111), Pd(111) and Ni(111) cases, which were chosen due to their diverse electronic structure according to the relative wide span covered by their d-band centers (*vide infra*). For the carboxylate and thiolate cases, the "lost" proton was bound on the opposite side of the slab. Nonetheless, this resulted in little effect on the catalyst electronic structure (Table S1) and binding energies of small chemical species (Table S2). At this point let us note that as shown in **Fig. 1,** MOF linkers at the interface "bridge" the NP surface and MOF nodes. However, while the latter may indirectly affect the electronic structure of the NP by altering that of the surface-bound linker, this effect is neglected here.

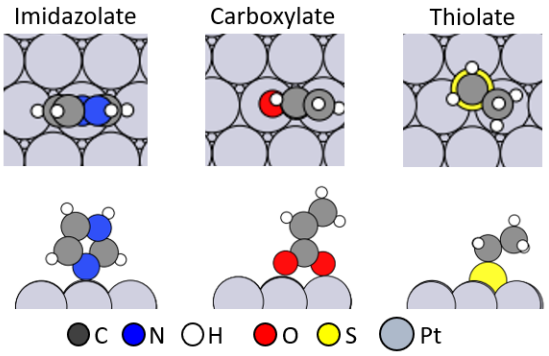

Figure 2. Optimized organic linker binding configuration on Pt(111) surface. Analogous configurations were obtained on Au, Cu, Pd, and Ni.

In earlier work,[34] we found the binding of methyl imidazole to Pt(111) to be stronger than the binding of N-vinylpyrrolidone (VP, the monomer of PVP). This finding supported the displacement of PVP—which enshrouds the Pt surface at the start of "bottle-around-ship" Pt@ZIF-8 synthesis—by methyl imidazole, which then binds directly to the Pt nanoparticle. To extend this comparison to other potential NP@MOF systems, we compared the calculated binding energies of the studied coordinating moieties on different metal surfaces relative to those for VP (**Table 1**). In these calculations, VP was constrained to remaining perpendicular to the metal surface and was found to interact more strongly with the O atom on a top site. The binding strength of imidazole and VP were relatively close, but VP only coordinated to the metal more strongly (by 7 kJ/mol) than imidazole in the Cu case. This suggests that interfaces similar to the one characterized in Pt@ZIF-8 are probable to occur in other NP@ZIF systems. Furthermore, we found both carboxylate and thiolate coordination to be far stronger than that of N-vinylpyrrolidone, which suggests that similar NP/MOF interfaces (where organic linkers coordinate directly to the encapsulated NP) are also likely encountered with carboxylate-based (and thiolate-based) MOFs.

Table 1. Binding energy of organic linker to metal surface (kJ/mol). I = imidazole, C = carboxylate, T = thiolate, N = N-vinylpyrrolidone.

Metal	Organic linker			
	I	C	T	N
Au	-78	-507	-496	-39
Cu	-91	-647	-622	-98
Pt	-204	-693	-696	-143
Pd	-140	-657	-715	-94
Ni	-123	-672	-726	-100

Thiolate binding was weaker than carboxylate binding on the metals with the higher d-band centers ε_d (Cu, Au) and weaker otherwise (Pt, Pd, Ni). Thiolate binding strength (Ni > Pd > Pt > Cu > Au) linearly correlates ($R^2 \sim 0.89$) with the d-band center position of the bare surface, with the binding strength increasing with higher d-band center (see calculated d-band centers in **Table S1**). Such correlation is much weaker for carboxylate ($R^2 \sim 0.65$), and non-existent for imidazole ($R^2 \sim 0.17$), primarily because Pt is an outlier that results in the strongest carboxylate/imidazole binding despite an intermediate d-band center (ε_d = -2.24 eV) among tested metals. Note that we did not include ZPE corrections in **Table 1**, which could somewhat affect calculated binding energies.[48] Furthermore, since the energies are calculated at the absolute zero, potential temperature effects are not considered in the above discussion.

Organic linker electronic effects. That catalyst encapsulation in MOFs can affect reaction pathways due to constraints on reactant orientation is rather apparent. However, it is not as clear whether judicious choice of MOF composition can be a way to modulate the catalyst electronic structure, and in turn activity and selectivity (which is known to occur when the active sites are embedded in the MOF[49,50]). Thus, to examine the impact of the linker coordination on the catalyst electronic structure, we start with an analysis of charge transfer (**Fig. 3**). The observed reduction of the catalyst surface upon coordination of imidazole is consistent with the electron-donating character of this linker. On the other hand, the oxidation of the catalyst surface upon coordination of carboxylate is consistent with the electron-withdrawing character of the linker oxygen atoms.

Within the same periodic table group (group 10 or 11), the higher the catalyst d-band center, the more electrons the linkers tend to retain or gain. For thiolate, for which we find an electron donating/withdrawing character between carboxylate and imidazole, only the metals with the highest d-band center within each group (i.e. Ni and Cu) end up oxidized due to linker coordination. For all cases, we inspected whether there was a correlation between electron transfer and binding energy. For imidazole, there is a weak correlation ($R^2 \sim 0.55$) between linker binding energy and electron transfer. However, for carboxylate and thiolate, there is no correlation at all between binding energy and electron transfer ($R^2 < 0.01$).

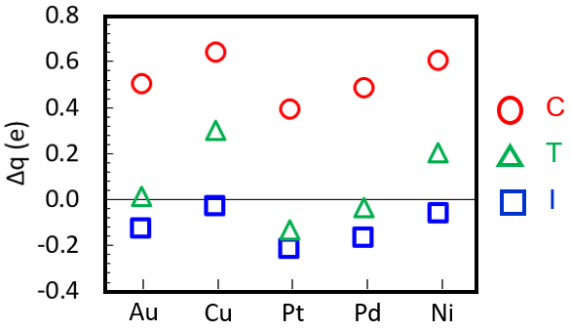

Figure 3. Charge transfer (q) from organic linker (I: imidazolate, C: carboxylate, T: thiolate) to surface. d-band center position (ε_d) for reference bare metal surface moves closer to the Fermi level from left to right.

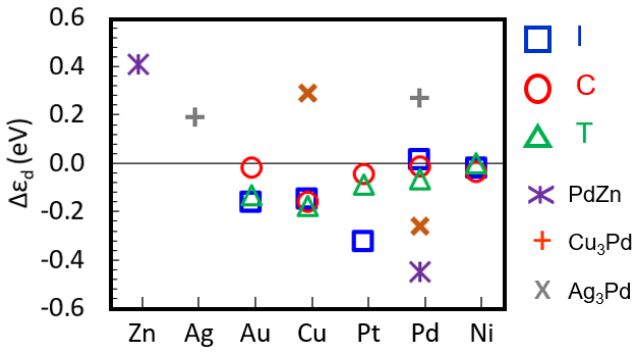

Figure 4. Shift in the d-band center ($\Delta\varepsilon_d$) of surface atoms either due to organic linker coordination (I: imidazolate, C: carboxylate, T: thiolate) or alloying. d-band center position (ε_d) for reference bare metal surface moves closer to the Fermi level from left to right.

According to the d-band model of Hammer and Norskov[51], the d-band center is the primary electronic factor controlling the binding strength of an adsorbate to a metal—although it is certainly not the only factor.[52-55] Thus, we analyzed was how the position of the d-band center was affected by the coordination of the linker as doing so could provide insights on how the binding of small species to the catalyst is expected to change due to MOF encapsulation. The metals studied here cover a wide range of d-band configurations as characterized by their d-band center, ε_d. **Fig. 4** shows the shift in d-band center position ($\Delta\varepsilon_d$) induced by linker coordination. We did not find any clear correlation between d-band center shifts and original d-band center positions, linker binding energies, or electron transfer upon linker coordination. However, we observe that regardless of whether the linker is donating (reducing) or withdrawing (oxidizing) electrons to or from the surface, upon coordination, the d-band center experiences a downward shift in all metals.

Although not quantified in this section, the downward shift in d-band center is expected to impact binding energies of small adsorbates. As a reference, we also inspected the shift in the d-band center due to alloying. To do so, we calculated these shifts *for each component* in the alloys studied by Getman and Zhu[31]: PdZn, $PdAg_3$ and $PdCu_3$, and added them to **Fig. 4.** The extent of the shifts due to alloying are consistent with values reported in the literature for other alloys.[56-58] One significant contrast between "alloy-induced" and "linker-induced" shifts is that upward shifts were only observed in the alloying cases. Additionally, we noticed that, at least where the comparison was possible (i.e. Cu, Pd), the alloy-induced shifts were larger in magnitude the (linker) coordination-induced ones.

Table 2. DFT-calculated data on CO adsorption on bare (linker-free) (111) surfaces, along with reference experimental data. Vibrational frequencies (**ν**) in cm^{-1}, C-O bond distance $d_{C\text{-}O}$ in Å, and CO charge (q_{CO}) in e. Parenthesis indicate interrogated binding site: t = top, f = fcc hollow, b = hcp hollow.

	DFT-calculated data			Exp. data	
Metal	**ν**	**$d_{C\text{-}O}$**	**q_{CO}**	**ν**	Ref.
Au (t)	2053	1.15	0.04	2060	[59]
Cu (t)	2001	1.16	-0.15	2070	[60]
Pt (t)	2073	1.16	0.05	2090	[61]
Pd (f)	1776	1.19	-0.22	1850	[62]
Ni (h)	1775	1.19	-0.36	1810	[63]

Impact of linker coordination on CO binding. Before examining the impact of linker coordination to the metal on the binding of several small adsorbates, we will focus on the impact on the binding of CO. We do so because the binding of CO can be relevant to experimental characterization of NP@MOFs systems. Indeed, the susceptibility of CO vibrational frequencies to changes in binding environment and electronic structure is commonly exploited in catalyst characterization via DRIFTS experiments. More recently, coupling of spectroscopic experiments and DFT calculations to elucidate atomistic details in MOF and zeolite systems have been reported as well.[64,65] Thus, CO sorption and spectroscopic measurements emerge as a viable tool to help understand MOF/NP interfaces and relevant electronic effects. In earlier work,[49] the measured redshift of C=O stretching frequency upon Pt encapsulation in ZIF-8—which matched the redshift in C=O stretching frequency when CO binds Pt(111) in the presence of coordinated methyl imidazole—was supporting evidence of an NP/MOF interface where linker directly coordinate to the catalysts surface. Experimental detection of similar shifts in other NP@MOFs according to predicted shifts based on interface models (such as the model here) could further corroborate postulated interface structures.

As a starting point, **Table 2** lists the calculated vibrational frequencies for CO on bare (111) surfaces. Since DFT is known to have trouble correctly predicting the correct binding site for CO,[66] on each surface, we placed CO on the binding site reported in experiments. The calculated frequencies are in reasonable agreement with experiments, with the largest deviations for Cu and Pd. Then, we determined how the properties of adsorbed CO (in the same binding site) change in the presence of the linker relative to the bare surface (**Table S4**). With the exception of Au and Cu with coordinated carboxylate, a redshift in C-O stretching frequency was observed in all cases. As expected, for each individual case, a redshift (or blueshift) in C-O stretching frequency was concomitant with an increase (or decrease) in the C-O bond distance. Considering all cases together, there is a strong correlation ($R^2 \sim 0.95$) between frequency shift ($\Delta\nu$) and change in C O bond distance ($\Delta d_{C\text{-}O}$) (**Fig. 5**, bottom). Interestingly, although weaker ($R^2 \sim 0.61$), there is a correlation between change in C¬O bond distance and the change in the amount of charge transferred (Δq_{CO}) (**Fig. 5**, top). An increase in the amount of charge transferred back to bound CO (due to linker coordination) tends to increase the stretch in the C-O bond. This observation is consistent with the Blyholder model,[67] where back-donated electrons go to CO antibonding orbitals, hence destabilizing the C-O bond.

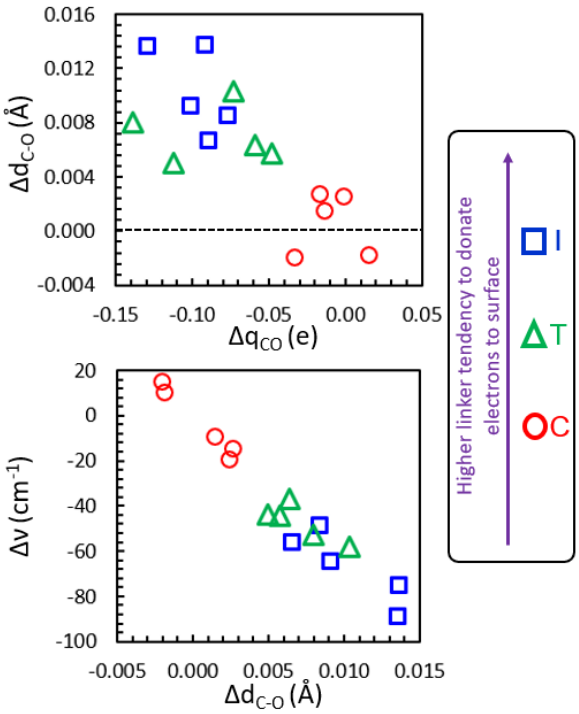

Figure 5. Changes in metal-surface bound CO geometry, electronics, and vibrations upon due to presence of organic linker**.** Changes provided for relative to property in bare surface (linker-free) cases. a) Change in C-O distance versus change in CO charge. b) Change in CO vibrational frequency versus change in C-O distance.

The above observations implicate that DRIFTS experiments on a synthesized NP@MOF could shed light on electron transfer effects between the MOF and the NP. Namely, redshifts in C-O stretching more than 50 cm^{-1} probably indicate electron donation happening from the MOF to the NP, while redshifts less than 50 cm^{-1} (or blueshifts) probably indicate electron withdrawal by the MOF from the NP. In turn, electron withdrawal or donation inferred from the experiments, can be used to support whether the MOF/NP interface structure is consistent with the interface model considered in this work. Notice that imidazole coordination leads to stronger redshifts than carboxylate coordination as the former linker reduces the surface while the latter linker oxidizes it.

Table 3. Binding energies, E_{ads} (kJ/mol), of small chemical species on bare (linker-free) (111) surfaces. Tested binding site indicated in superscript: *t* = atop, *f* = fcc hollow, *h* = hcp hollow, *b* = bridge

	Metal				
Species	**Au**	**Cu**	**Pt**	**Pd**	**Ni**
CO*	-43 $^{(t)}$	-101 $^{(t)}$	-205 $^{(t)}$	-221 $^{(f)}$	-205 $^{(f)}$
CH_3*	-156 $^{(t)}$	-179 $^{(f)}$	-264 $^{(t)}$	-212 $^{(t)}$	-214 $^{(f)}$
OH*	-190 $^{(f)}$	-320 $^{(f)}$	-219 $^{(b)}$	-260 $^{(f)}$	-320 $^{(f)}$
H*	-209 $^{(f)}$	-254 $^{(f)}$	-273 $^{(f)}$	-279 $^{(f)}$	-273 $^{(f)}$
N*	-254 $^{(f)}$	-396 $^{(f)}$	-486 $^{(f)}$	-478 $^{(f)}$	-519 $^{(f)}$
O*	-313 $^{(f)}$	-480 $^{(f)}$	-425 $^{(f)}$	-430 $^{(f)}$	-515 $^{(f)}$
C*	-451 $^{(f)}$	-519 $^{(f)}$	-707 $^{(f)}$	-697 $^{(f)}$	-664 $^{(f)}$

Impact of linker coordination on binding of small adsorbates. Previous microkinetic model-based 2D "volcano" plots for computational screening of NP@MOFs,[31] were i) built on scaling relationships (as typical in catalyst high throughput screening), and ii) did not consider linker coordination-driven electronic effects on catalysts and their consequences on reaction energetics. Thus, we now proceed to inspect the impact of these electronic effects on the binding of small adsorbates (CO*, CH_3*, OH*, H*, N*, O*, C*). We selected these adsorbates because they are the basis of a number of published scaling relationships,[68-70] including those published by Zhu and Getman[31] for screening of NP@MOFs for selective n-butane oxidation to 1-butanol, which are based on the binding of OH* and C*.

As a starting point, **Table 3** summarizes the binding energies, E_{ads}, of the studied adsorbates on the linker-free surfaces. To reduce the number of calculations, we only explored the binding sites known to be most stable for each adsorbate. **Table 3** does not include ZPE corrections. This was partly motivated by tests (**Table S3**) showing that the effect of linker coordination on ZPE is negligible. Thus, ZPE corrections do not influence our analysis on how adsorbate binding *changes* due to linker coordination on the metal surface (although they can affect individual E_{ads} values by 8-27 kJ/mol). Although we used the PBE functional, our obtained binding energies and trends on bare surfaces are in reasonable agreement with data from a series of publications by Mavrikakis and coworkers[71-75] that primarily use the PW91 functional, as well as data from other authors.[68,76] In Au, the binding strength follows the trend C* > O* > N* > H* > OH* > CH_3* > CO. In other metals, some adsorbates swap positions (e.g. O* and N* in higher d-band metals, OH* and H* in 3d metals). The strongest binding in each surface occurs for C*, and the weakest binding for CO*.

Charge analysis (**Fig. S7**) shows that in all instances (except for CO* on Au and Pt) the adsorbate gains electrons (the surface oxidizes) upon binding. Within the same metal group, surface oxidation with each adsorbate binding increases as the metal period decreases. Within the same metal period, surface oxidation increases as the metal group increases. In Au, surface oxidation by adsorbate binding follows the trend O* > N* > C* > OH* > CH_3 > H* > CO*, which generally holds in the other studied metals. The adsorbate charge was a critical part of a multivariate linear regression ($R^2 \sim 0.85$) to predict binding energy (in kJ/mol) resulting in:

$$E_{ads} = -280.5 - 97.7n - 68.2\varepsilon_d + 74.9q_{ads} \quad (1)$$

where n is the number of bonds the adsorbate needs to make to complete valency (0 for CO, 1 for OH, H, CH_3, 2 for O, 3 for N, and 4 for C), ε_d is the d-band center of the metal and q_{ads} is the charge of the adsorbate. Expectedly, binding tends to be stronger the more "unsaturated" the adsorbate and the higher the d-band center of the metal are. **Eq. 1** also indicates that the more electrons the adsorbate gains from the surface, the stronger the binding is.

Once the organic linker coordinates to the metal surface, charge transfer between the metal and the adsorbate changes according to some rather clear trends (**Fig. S11**).

Imidazole coordination leads to some of the electrons donated by the linker, hence enhancing electron gains by the bound adsorbates. Carboxylate coordination, on the other hand, results in a more electron-depleted surface, hence inhibiting electron transfer to the adsorbates. The change in binding energy for the studied species is summarized in **Fig. 6,** which is based on the data in **Tables S4-S6**.

In 60% of the tested cases, the binding of the adsorbate was weakened due to linker coordination. This tendency for binding destabilization is partly explained by the observed downward shifts in d-band centers upon linker coordination (**Fig. 4**). However, non-bonded interactions with the coordinated linker can also stabilize/destabilize adsorbate binding. Analyzing the linker cases separately, adsorbate binding was weakened by coordination of imidazole, carboxylate, and thiolate in 47%, 59% and 60% of the cases, respectively. Regardless of whether binding was stabilized or destabilized, in 60% of the tested cases, adsorbate binding energies only changed within 10 kJ/mol (69% of carboxylate cases, 52% of imidazole cases, 48% of thiolate cases).

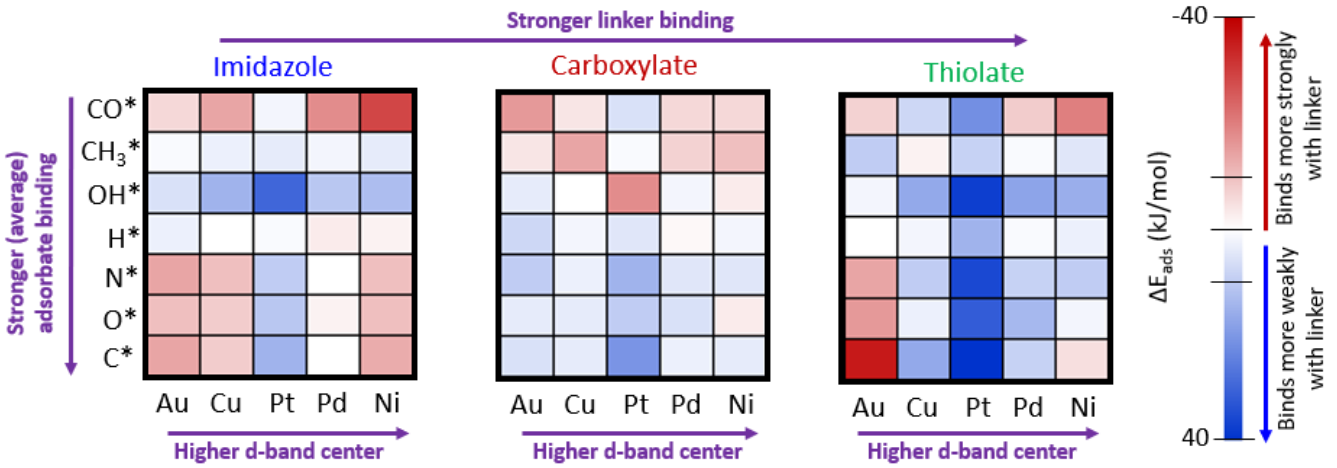

Figure 6. Change in adsorbate binding energy ($\Delta E_{ads} = (E_{ads})_{with\ linker} - E_{ads}$) due to the coordination of the linker to the catalyst surface. The amount of change is indicated by color consistent with the right color bar. Data for this figure was obtained from Tables S3-S5. The binding energies E_{ads} to obtain ΔE_{ads} are calculated in the same type of binding site.

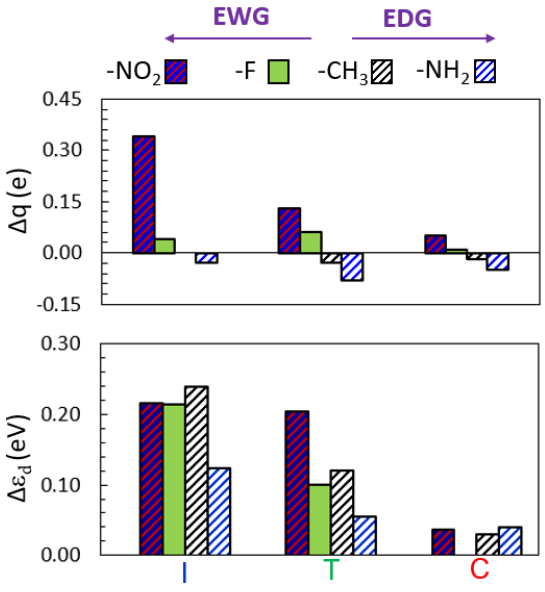

Figure 7. Electronic effects on metal surface due to functionalization of coordinating organic linker. Top: Change in the charge of the metal surface due to linker functionalization. Bottom: Change in the metal d-band center due to linker functionalization.

Effect of linker functionalization. One of the appeals of MOFs is that even more crystal composition variations can be obtained due to variations in the organic linkers by functionalization. To explore functionalization effects, we focused on Pt, because this metal seemed to be significantly more susceptible to linker coordination effects than Au, Cu, Pd and Ni. Accordingly, the linkers tested here were functionalized with electron donating (-NH_2 and -CH_3) and withdrawing (-F and -NO_2) groups. Functionalization with electron withdrawing (EWG) groups strengthened the coordination of the linker to the surface, while the effect of functionalization with electron donating (EDG) groups was mixed (**Table S8**). This could be indicative of NP@MOF synthesis being facilitated by functionalization with EWG groups.

In terms of electronic effects, we found the introduction of the EWG and EDG groups on the linker to have the expected effect on charge transfer between linker and metal surface. Specifically, functionalization with EWG groups (-NO_2 and -F) led to the linker gaining more electrons than the unfunctionalized linker, while the opposite was true when functionalizing with EDG groups (-CH_3 and -NH_2) (**Fig. 7**, top). Interestingly, regardless of whether EWG or EDG groups were introduced, we found that functionalization led to an *upward* shift in the metal d-band center, relative to its position when the unfunctionalized linker was coordinated.

Notably, however, in 94% of instances, linker functionalization only led to changes in adsorbate binding energy within 10 kJ/mol (**Table S9**). Furthermore, in numerous cases (about 50%) functionalization only led to changes within 2 kJ/mol. This is apparent in the parity plot in **Fig. 8**, where the majority of points virtually fall on the parity line, with a few outlier exceptions. Inspecting the outliers (e.g. OH* binding nearly 100 kJ/mol more strongly when thiolate was

functionalized with -NH_2), we find that pronounced changes in binding energies upon linker functionalization are not due to electronic effects induced by the linker on the metal. Instead, the cause for the pronounced difference is the direct interaction of the adsorbate with the functional group. The interaction can be attractive such as in hydrogen bonds typically formed by OH*, or repulsive as in hindrance occurring (sometimes) to CH_3* and CO*. A couple binding configurations where hydrogen bonding occur are shown in **Fig. 8** (it is worth noting that in these cases, the adsorbate binding site also changed spontaneously). Intriguingly, these configurations show a potential way to break scaling relationships at MOF/NP interfaces. For instance, NP encapsulation with an amino linker could have a small effect on O* binding but could, on the other hand, significantly strengthen OH* binding.

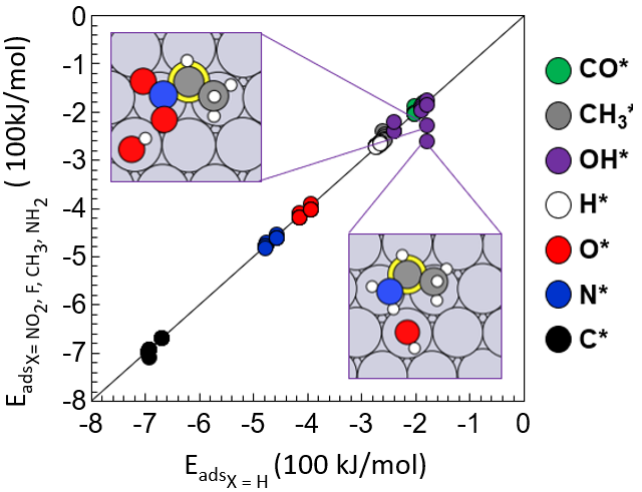

Figure 8. Parity plot comparing the binding energy of adsorbates in the presence of the coordinating unfunctionalized linker vs in the presence of the functionalized linker. Inset shows two outlier cases, where adsorbate binding was strengthened more than 70 kJ/mol due to hydrogen bonding.

Implications on screening of MOF-encapsulated catalysts. The relationship between binding energies determines scaling relationships that are used to produce 2D volcano plots, on which screened catalysts are located to reveal their expected performance. Ignoring electronic effects during catalyst screening of NP@MOFs can raise two problems: i) the underlying 2D volcano plot obtained from scaling relationships could be faulty, and/or ii) the location of catalyst compositions within the plot could be incorrect. To examine the first potential problem, we examined how scaling relationships between binding energies are affected by linker coordination.

If linker coordination had a commensurate effect on binding energies (e.g. a 10% increase in all binding energies), scaling relationships would not be affected. Accordingly, the descriptor-based 2D volcano plots produced exploiting these relationships without consideration of electronic effects would still be meaningful for MOF-encapsulated catalyst screening. However, since it is apparent that the effect of linker coordination is not homogenous across all studied systems (**Fig. 4**), then the impact of linker coordination on scaling relationships needs to be directly examined. To this end, we calculated scaling relationships among all tested adsorbates (**Fig. S12**) using all available binding energy data (type *a*) and compared them with relationships obtained excluding the cases where there was linker coordination on the surface (type *e*).

Table 4. Average difference $(\Delta E_{ads})_{ave}$ in kJ/mol for binding energies obtained from scaling relationships derived on bare surfaces (type *e*) vs. from scaling relationships derived on surfaces with coordinated linkers (type *a*). Detailed scaling relationships shown in Fig. S12.

Relationship	$(\Delta E_{ads})_{ave}$	Relationship	$(\Delta E_{ads})_{ave}$
CO* vs C*	-7	CO* vs N*	-11
CH_3* vs C*	-1	CH_3* vs N*	0
OH* vs C*	7	OH* vs N*	5
H* vs C*	-1	H* vs N*	-2
N* vs C*	1	CO* vs H*	-9
O* vs C*	-2	CH_3* vs H*	-1
CO* vs O*	-10	OH* vs H*	4
CH_3* vs O*	2	CO* vs OH*	-11
OH* vs O*	5	CH_3 vs OH*	1
H* vs O*	1	CO* vs CH_3*	-7
N* vs O*	-2		

When examining percentual deviations of the slopes and intersects of the 21 calculated scaling relationships individually, we find them to be less than 10% in most cases. However, in a few instances where the slope or intercept are small numbers, the percentual deviations are much higher. Thus, to better quantify the effect of electronic effects on scaling relationships, we calculated the average absolute deviation between binding energies calculated with type *a* and type *e* scaling relationships, $(\Delta E_{ads})_{ave}$. We calculated this metric using the range of binding energies that was used to derive the scaling relationships in the first place. As evident from **Table 4**, the deviations are rather minor, with the largest deviations tending to occur when CO* is involved. Note that linker coordination effects are a form of coverage effects. However, contrary to other works[77,78] where coverage effects are found to significantly impact scaling relationships, here the impact looks minor likely due to the "coverage" of the linker being relatively low. The above data suggest that 2D volcano plots for screening of NP@MOFs obtained based on scaling relationships that neglect linker-coordination-related electronic effects could present some minor distortions relative to plots that would consider these effects. However, the former plots are likely useful to rapidly narrow down promising catalyst compositions for the application of choice.

To examine the second potential problem with neglecting linker-coordination-related electronic effects (i.e. location of a catalyst composition on a 2D volcano plot being incor-

rect), we reproduced the 2D volcano plots by Zhu and Getman[31] for n-butane oxidation, which were produced from calculations under generic steric constraints (no electronic effects due to linker coordination). To do so, we used their published microkinetic model and scaling relationships, which are based on OH* and C* formation energies (calculated from binding energies) with no ZPE corrections. To include catalyst compositions studied here, we extended the range of the plots so they would include the corresponding formation energy values. Note that because no free energies were used, some temperature effects captured by the TS product are ignored. As reference, some tests in platinum showed the TS product to be 2-27 kJ/mol (depending on the species) at 150 C, which was the reaction temperature considered here. The reactions for the microkinetic model are listed in **Table S10**. Briefly, O_2 and H_2O adsorb on the catalyst surface to produce O* and OH*. *n*-butane adsorbs as well and can forms either 1-butanol, butanal, or butene through oxidation reactions. The goal is to find a catalyst that actively and selectively produces 1-butanol, because this shows a catalyst architecture that can produce valuable primary alcohols from cheap natural gas feedstock.

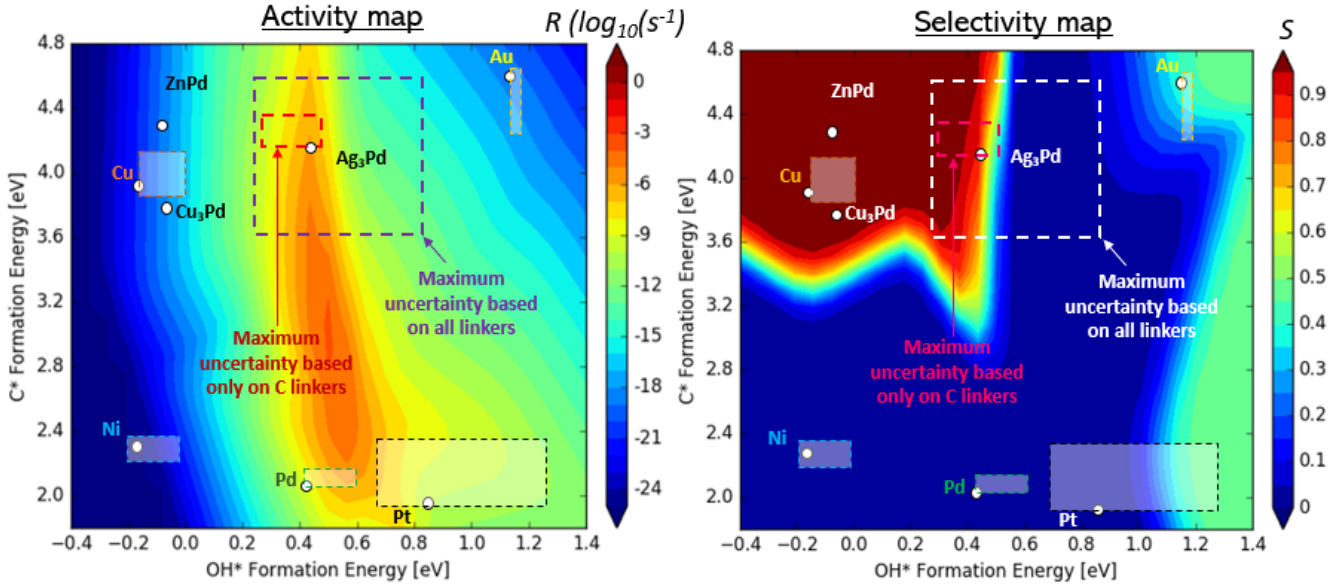

Figure 9. 2D volcano plots illustrating the activity (left) and selectivity (right) of various catalyst compositions.

To place the catalysts on the volcano plots for activity (**Fig. 9** left) and selectivity (**Fig. 9** right), the formation energies in **Table S11** were used (which were obtained using our calculated binding energies). The selectivity was only calculated for butanal versus butene formation, as 2-butanol formation is assumed to be prevented by steric constraints. The plots are calculated at 150 C and partial pressures P_{butane} = 3750 kPa, P_{H2O} = 456 kPa, P_{O2} = 2 kPa. The "point" for each catalyst composition is given by the formation energy of OH* and C* on its surface without considering electronic effects due to linker coordination (i.e. on the bare surface). Then, to account on how *electronic* effects due to encapsulation in a MOF could alter the location of the catalyst composition on the volcano plot, we added an "uncertainty box" for the pure metals. For each metal, this box encompasses the region where OH* and C* formation energies are within the maximum deviation in OH* and C* stability due to linker coordination, as per the data in **Fig. 6** and **Tables S4-S6**.

For most metals, the uncertainty box is relatively small, indicating, for instance, that regardless of potential electronic effects upon encapsulation in a MOF, Ni, Cu, and Au (and Ag) would present low activity for n-butane oxidation, with Ni and Au additionally presenting low selectivity for 1-butanol formation. For Pt, however, the uncertainty box is relatively large, expanding 0.36 eV above and 0.17 eV below the OH* formation energy on bare Pt, and 0.39 eV above the C* formation energy on bare Pt. The large uncertainty box for this metal indicates that although Pt has an intrinsic (i.e. without electronic effects) of only 10^{-10} s^{-1}, there is a 14% probability that encapsulation in some MOF may raise activity to 10^{-8} s^{-1} or above. However, regardless of encapsulation, selectivity for 1-butanol is bound to stay below 0.4. Examining a metal such as Pd, it appears that alloying with Zn, Cu, or Ag has a much drastic effect on reaction energetics on a metal—hence on the location of a metal on the volcano plot—than electronic effects due to encapsulation would.

For the pure metals the uncertainty boxes were drawn based on DFT calculations explicitly examining the impact of electronic effects. For other compositions such as the alloys we however did not perform such calculations. Without considering electronic effects, one of these alloys, Ag_3Pd seems a promising catalyst composition with a selectivity of 0.75 and an activity of 10^{-6} s^{-1}. To provide a probability that Ag_3Pd remains an attractive catalyst despite potential electronic effects upon encapsulation in a MOF, we considered a worst-case scenario. Namely, that the deviation in C* and OH* formation energies (positive and negative) can all be as dramatic as the worst case in any of the studied pure metals. Under this scenario, the probability of Ag_3Pd retaining a selectivity above 75% and an activity above 10^{-8} s^{-1} is ~30% in both cases. On the other hand, if we only considered the deviations due to carboxylate coordination, there is a ~70%

probability that Ag_3Pd encapsulated in a carboxylate MOF would have an activity higher than 10^{-8}, and ~85% probability that selectivity remains above 75%.

Can uncertainty be reduced? The uncertainties above, are based on worse-case scenarios. A relevant question is whether there are ways—compatible with high throughput screening—to have a better idea of where an encapsulated catalyst composition would fall in plots like **Fig. 9** when considering potential electronic effects by the MOF. In other words, the question is whether there is a way to better anticipate the binding energy of a species of interest in the presence of the relevant linker, without performing the actual DFT calculation. Since a promising, fast method to predict binding energies on catalyst surfaces is machine learning, we inspected reported accuracies in some recent efforts in this area.[79-82] Accuracies in the 5-20 kJ/mol (0.05-0.2 eV) range have been reported, which are promising when you consider the size of the uncertainty region based on all linkers, as shown for Ag_3Pd in **Fig. 9**. However, machine learning predictions have so far been carried on bare catalyst surfaces, but not on surfaces with coordinated linkers. Accordingly, we took a first look into predicting adsorbate binding energies on surfaces with coordinated linkers.

It should be clear, however, that our current dataset is not large enough to train a robust, generalizable machine learning model. On the other hand, we can, for instance, inspect what kind of descriptors could be useful to develop such model. A task that it is well suited for a gradient boosted machines (GBM) model.[83] Although GBMs can be outperformed by deep neural networks once the training dataset surpasses a certain size, GBMs outperform the latter when datasets are smaller, and provide useful information on descriptor importance. Note that **Eq. 1** already hints that binding relates to adsorbate "unsaturation" (n), as well as factors influenced by linker coordination such as d-band center (ε_d) and electron transfer to the adsorbate (q_{ads}). The latter, however, is not a useful descriptor for a machine learning model, because finding its value requires the kind of DFT calculation that one is trying to avoid in the first place.

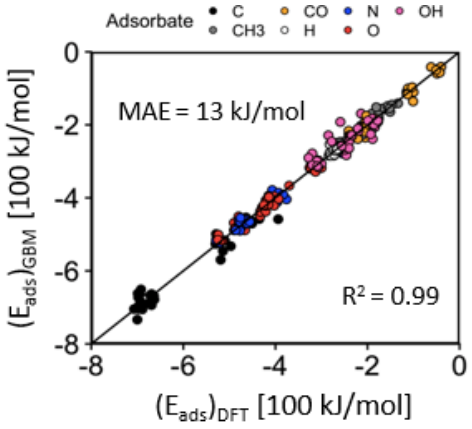

Figure 10. Binding energy predictions by a GBM (gradient boosted machines) model vs DFT calculations on catalyst surfaces with and without coordinating linkers.

Ultimately, our most successful GBM model (see details in the Supplementary Information) trained to predict binding energies used the following properties of the adsorbate and the surface: the numbers of bonds the adsorbate needs to make to complete valency (n), the surface d-band center (ε_d), the electronegativity of the adsorbate binding atom (χ_{ads}), the electronegativity of the surface binding site (χ_{site}), the charge of the surface (q_{surf}), the dispersion parameter of the surface atoms (C_{6surf}) and the sum of the dispersion parameters of the atoms of the coordinating linker ($\Sigma C_{6linker}$). Analysis of the GBM model reveals that the binding energy is mostly determined by n (71% importance), followed by ε_d (14%) and χ_{ads} (8%), with the remaining 7% explained by the remaining variables. Note that we expected χ_{ads}, χ_{surf}, and q_{surf} to play the role of q_{ads}, so it is reassuring to see these variables playing a role in the prediction. When comparing the predictions of the GBM model with the actual DFT calculation, the mean absolute error (MAE) for the GBM predictions was 13 kJ/mol, which is within the accuracy range of previously mentioned machine learning models.[79-82]

■ CONCLUSIONS

Using approximated NP/MOF interface models, DFT calculations were used to investigate MOF-originated electronic effects on encapsulated NPs in NP@MOF hybrid catalysts. The nature and extent of linker-induced electronic effects on the metal was found to be modulated by the chemistry of the linker, and to typically weaken the binding energies of common "catalytic" species. More generally, however, changes in binding energies (positive or negative) tended to stay within 10 kJ/mol and only led to slight changes in scaling relationships between binding energies of these species. An implication of the findings herein is that they suggest that one potential way to screen NP@MOF catalysts for reactions of interest (at least when the MOF is "innocent" to reactive intermediates) could be to follow a hierarchical strategy. First, key descriptors and scaling relationships could be determined using full "mechanistic" DFT calculations with MOF-independent "generic" steric constraints, which could then be used to construct descriptor-based activity/selectivity volcano plots. Then, the exact placement of a promising NP composition on these plots could be refined by additional calculations considering MOF-specific effects (potentially even using machine learning). Ultimately, confidence in attempting to encapsulate a NP composition in a MOF for experimental testing will depend on the "roughness" of the relevant volcano plot and the position of the NP composition in the latter. In other words, it will depend on how sensitive the predicted performance of an encapsulated NP is to small changes in descriptor energy.

SUPPLEMENTARY INFORMATION

Electronic Supplementary Information (ESI) available: Snapshots of all optimized geometries. Scaling relationships. Additional data related to charge transfer. Reactions and descriptor values for microkinetic model. Details for training of GBM model.

AUTHOR INFORMATION

Corresponding Author

* dgomezgualdron@mines.edu

Author Contributions

‡ These authors contributed equally

Funding Sources

NSF CAREER.

ACKNOWLEDGMENTS

D.A.G.-G. acknowledges funding from NSF CAREER (CBET 1846707). Simulations were made possible by the Mio supercomputer cluster at Colorado School of Mines. We thank Prof. Rachel Getman and Mr. Jiazhou Zhu at Clemson University for useful discussions about the microkinetic model for n-butane oxidation.

REFERENCES

1 U.S. Energy Information Administration, Industrial sector energy consumption, *International Energy Outlook*, 2016, 113-126.

2 D. S. Sholl and R. P. Lively, Seven chemical separations to change the world, *Nature*, 2016, **532**, 435-437.

3 J. M. White and J. Bercaw, Opportunities for Catalysis in The 21st Century. A report from the Basic Energy Sciences Advisory Committee, 2002.

4 S. Shoda, H. Uyama, J. Kadokawa, S. Kimura and S. Kobayashi, Enzymes as Green Catalysts for Precision Macromolecular Synthesis, *Chem Rev*, 2016, **116**, 2307-2413.

5 P. Hu, J. V. Morabito and C. K. Tsung, Core-Shell Catalysts of Metal Nanoparticle Core and Metal-Organic Framework Shell, *Acs Catal*, 2014, **4**, 4409-4419.

6 K. B. Schowen, H. H. Limbach, G. S. Denisov and R. L. Schowen, Hydrogen bonds and proton transfer in general-catalytic transition-state stabilization in enzyme catalysis, *Biochim Biophys Acta*, 2000, **1458**, 43-62.

7 S. T. Marshall, M. O'Brien, B. Oetter, A. Corpuz, R. M. Richards, D. K. Schwartz and J. W. Medlin, Controlled selectivity for palladium catalysts using self-assembled monolayers, *Nat Mater*, 2010, **9**, 853-858.

8 S. H. Pang, C. A. Schoenbaum, D. K. Schwartz and J. W. Medlin, Directing reaction pathways by catalyst active-site selection using self-assembled monolayers, *Nat Commun*, 2013, **4**, 2448.

9 K. R. Kahsar, D. K. Schwartz and J. W. Medlin, Control of metal catalyst selectivity through specific noncovalent molecular interactions, *J Am Chem Soc*, 2014, **136**, 520-526.

10 S. T. Marshall, D. K. Schwartz and J. W. Medlin, Adsorption of oxygenates on alkanethiol-functionalized Pd(111) surfaces: mechanistic insights into the role of self-assembled monolayers on catalysis, *Langmuir*, 2011, **27**, 6731-6737.

11 B. Wu, H. Huang, J. Yang, N. Zheng and G. Fu, Selective hydrogenation of alpha,beta-unsaturated aldehydes catalyzed by amine-capped platinum-cobalt nanocrystals, *Angew Chem Int Ed Engl*, 2012, **51**, 3440-3443.

12 S. H. Pang, C. A. Schoenbaum, D. K. Schwartz and J. W. Medlin, Effects of Thiol Modifiers on the Kinetics of Furfural Hydrogenation over Pd Catalysts, *ACS Catal*, 2014, **4**, 3123-3131.

13 L. D. Ellis, R. M. Trottier, C. B. Musgrave, D. K. Schwartz and J. W. Medlin, Controlling the Surface Reactivity of Titania via Electronic Tuning of Self-Assembled Monolayers, *ACS Catal*, 2017, **7**, 8351-8357.

14 G. Kumar, T. Van Cleve, J. Park, A. van Duin, J. W. Medlin and M. J. Janik, Thermodynamics of Alkanethiol Self-Assembled Monolayer Assembly on Pd Surfaces, *Langmuir*, 2018, **34**, 6346-6357.

15 C. A. Schoenbaum, D. K. Schwartz and J. W. Medlin, Controlling the surface environment of heterogeneous catalysts using self-assembled monolayers, *Acc Chem Res*, 2014, **47**, 1438-1445.

16 L. Y. Chen, H. R. Chen, R. Luque and Y. W. Li, Metal-organic framework encapsulated Pd nanoparticles: towards advanced heterogeneous catalysts, *Chem Sci*, 2014, **5**, 3708-3714.

17 G. Lu, S. Li, Z. Guo, O. K. Farha, B. G. Hauser, X. Qi, Y. Wang, X. Wang, S. Han, X. Liu, J. S. DuChene, H. Zhang, Q. Zhang, X. Chen, J. Ma, S. C. Loo, W. D. Wei, Y. Yang, J. T. Hupp and F. Huo, Imparting functionality to a metal-organic framework material by controlled nanoparticle encapsulation, *Nature Chem*, 2012, **4**, 310-316.

18 Y. Huang, Y. Zhang, X. Chen, D. Wu, Z. Yi and R. Cao, Bimetallic alloy nanocrystals encapsulated in ZIF-8 for synergistic catalysis of ethylene oxidative degradation, *Chem Commun*, 2014, **50**, 10115-10117.

19 H. Liu, L. Chang, C. Bai, L. Chen, R. Luque and Y. Li, Controllable Encapsulation of "Clean" Metal Clusters within MOFs through Kinetic Modulation: Towards Advanced Heterogeneous Nanocatalysts, *Angew Chem Int Ed Engl*, 2016, **55**, 5019-5023.

20 G. Li, S. Zhao, Y. Zhang and Z. Tang, Metal-Organic Frameworks Encapsulating Active Nanoparticles as Emerging Composites for Catalysis: Recent Progress and Perspectives, *Adv Mater*, 2018, **30**, e1800702.

21 V. R. Bakuru, D. Davis and S. B. Kalidindi, Cooperative catalysis at the metal-MOF interface: hydrodeoxygenation of vanillin over Pd nanoparticles covered with a UiO-66(Hf) MOF, *Dalton Trans*, 2019, **48**, 8573-8577.

22 K. Na, K. M. Choi, O. M. Yaghi and G. A. Somorjai, Metal nanocrystals embedded in single nanocrystals of MOFs give unusual selectivity as heterogeneous catalysts, *Nano Lett*, 2014, **14**, 5979-5983.

23 K. M. Choi, K. Na, G. A. Somorjai and O. M. Yaghi, Chemical Environment Control and Enhanced Catalytic Performance of Platinum Nanoparticles Embedded in Nanocrystalline Metal-Organic Frameworks, *J Am Chem Soc*, 2015, **137**, 7810-7816.

24 L. Dou, S. N. Wu, D. L. Chen, S. H. He, F. F. Wang and W. D. Zhu, Structures and Electronic Properties of Au Clusters Encapsulated ZIF-8 and ZIF-90, *J Phys Chem C*, 2018, **122**, 8901-8909.

25 J. Greeley, T. F. Jaramillo, J. Bonde, I. B. Chorkendorff and J. K. Norskov, Computational high-throughput screening of electrocatalytic materials for hydrogen evolution, *Nature Mater*, 2006, **5**, 909-913.

26 D. A. Gomez-Gualdron, Y. J. Colon, X. Zhang, T. C. Wang, Y. S. Chen, J. T. Hupp, T. Yildirim, O. K. Farha, J. Zhang and R. Q. Snurr, Evaluating topologically diverse metal-organic frameworks for cryo-adsorbed hydrogen storage, *Energy Environ Sci*, 2016, **9**, 3279-3289.

27 J. K. Norskov, T. Bligaard, J. Rossmeisl and C. H. Christensen, Towards the computational design of solid catalysts, *Nature Chem*, 2009, **1**, 37-46.

28 D. A. Gomez-Gualdron, S. T. Dix, R. B. Getman and R. Q. Snurr, A modelling approach for MOF-encapsulated metal catalysts and application to n-butane oxidation, *Phys Chem Chem Phys*, 2015, **17**, 27596-27608.

29 S. T. Dix, D. A. Gomez-Gualdron and R. B. Getman, Implications of sterically constrained n-butane oxidation reactions on the reaction mechanism and selectivity to 1-butanol, *Surf Sci*, 2016, **653**, 11-21.

30 S. T. Dix, J. K. Scott, R. B. Getman and C. T. Campbell, Using degrees of rate control to improve selective n-butane oxidation over model MOF-encapsulated catalysts: sterically-constrained Ag3Pd(111), *Faraday Discuss*, 2016, **188**, 21-38.

31 J. Z. Zhu and R. B. Getman, Reaction Pathways and Microkinetic Modeling of n-Butane Oxidation to 1-Butanol on Cu, Cu3Pd, Pd, Ag3Pd, and PdZn (111) Surfaces, *Ind Eng Chem Res*, 2018, **57**, 5580-5590.

32 X. L. Li, T. W. Goh, L. Li, C. X. Xiao, Z. Y. Guo, X. C. Zeng and W. Y. Huang, Controlling Catalytic Properties of Pd Nanoclusters through Their Chemical Environment at the Atomic Level Using Isoreticular Metal-Organic Frameworks, *ACS Catal*, 2016, **6**, 3461-3468.

33 J. Juan-Alcaniz, J. Gascon and F. Kapteijn, Metal-organic frameworks as scaffolds for the encapsulation of active species: state of the art and future perspectives, *J Mater Chem*, 2012, **22**, 10102-10118.

34 C. L. Whitford, C. J. Stephenson, D. A. Gomez-Gualdron, J. T. Hupp, O. K. Farha, R. Q. Snurr and P. C. Stair, Elucidating the Nanoparticle Metal Organic Framework Interface of Pt@ZIF-8 Catalysts, *J Phys Chem C*, 2017, **121**, 25079-25091.

35 G. Kresse and J. Hafner, Ab initio molecular dynamics for liquid metals, *Phys Rev B Condens Matter*, 1993, **47**, 558-561.

36 G. Kresse and J. Hafner, Ab initio molecular-dynamics simulation of the liquid-metal-amorphous-semiconductor transition in germanium, *Phys Rev B Condens Matter*, 1994, **49**, 14251-14269.

37 G. Kresse and J. Furthmuller, Efficiency of ab-initio total energy calculations for metals and semiconductors using a plane-wave basis set, *Comp Mater Sci*, 1996, **6**, 15-50.

38 J. P. Perdew, K. Burke and M. Ernzerhof, Generalized gradient approximation made simple, *Physical Review Letters*, 1996, **77**, 3865-3868.

39 S. Grimme, Semiempirical GGA-type density functional constructed with a long-range dispersion correction, *J Comput Chem*, 2006, **27**, 1787-1799.
40 K. M. Ho, C. L. Fu, B. N. Harmon, W. Weber and D. R. Hamann, Vibrational Frequencies and Structural-Properties of Transition-Metals Via Total-Energy Calculations, *Phys Rev Lett*, 1982, **49**, 673-676.
41 "Materials Studio" Accelyrs Software Inc. San Diego, CA 92121, USA, 2001-2011.
42 Y.-X. Yu, Prediction of Mobility, Enhanced Storage Capacity, and Volume Change during Sodiation on Interlayer-Expanded Functionalized Ti3C2 MXene Anode Materials for Sodium-Ion Batteries, *J Phys Chem C*, 2016, **120**, 5288-5296.
43 G. Henkelman, A. Arnaldsson and H. Jonsson, A fast and robust algorithm for Bader decomposition of charge density, *Comp Mater Sci*, 2006, **36**, 354-360.
44 W. Tang, E. Sanville and G. Henkelman, A grid-based Bader analysis algorithm without lattice bias, *J Phys-Condens Mat*, 2009, **21**.
45 A. J. Medford, C. Shi, M. J. Hoffmann, A. C. Lausche, S. R. Fitzgibbon, T. Bligaard and J. K. Norskov, CatMAP: A Software Package for Descriptor-Based Microkinetic Mapping of Catalytic Trends, *Catal Lett*, 2015, **145**, 794-807.
46 T. C. Narayan, T. Miyakai, S. Seki and M. Dinca, High charge mobility in a tetrathiafulvalene-based microporous metal-organic framework, *J Am Chem Soc*, 2012, **134**, 12932-12935.
47 A. Pathak, J. W. Shen, M. Usman, L. F. Wei, S. Mendiratta, Y. S. Chang, B. Sainbileg, C. M. Ngue, R. S. Chen, M. Hayashi, T. T. Luo, F. R. Chen, K. H. Chen, T. W. Tseng, L. C. Chen and K. L. Lu, Integration of a (-Cu-S-)n plane in a metal-organic framework affords high electrical conductivity, *Nature Commun*, 2019, **10**, 1721.
48 R. Gholizadeh, Y.X. Yu, N2O + CO reaction over Si- and Se-doped graphenes: An ab initio DFT study, *Appl. Surf. Sci*. 2015, **357**, 1187-1195
49 P. Liao, R. B. Getman and R. Q. Snurr, Optimizing Open Iron Sites in Metal-Organic Frameworks for Ethane Oxidation: A First-Principles Study, *ACS Appl Mater Interfaces*, 2017, **9**, 33484-33492.
50 A. S. Rosen, J. M. Notestein and R. Q. Snurr, Structure-Activity Relationships That Identify Metal-Organic Framework Catalysts for Methane Activation, *ACS Catal*, 2019, **9**, 3576-3587.
51 B. Hammer and J. K. Norskov, Electronic factors determining the reactivity of metal surfaces, *Surf Sci*, 1995, **343**, 211-220.
52 H. Xin and S. Linic, Communications: Exceptions to the d-band model of chemisorption on metal surfaces: The dominant role of repulsion between adsorbate states and metal d-states, *J Chem Phys*, 2010, **132**, 221101.
53 M. M. Montemore and J. W. Medlin, A unified picture of adsorption on transition metals through different atoms, *J Am Chem Soc*, 2014, **136**, 9272-9275.
54 H. L. Xin, A. Vojvodic, J. Voss, J. K. Norskov and F. Abild-Pedersen, Effects of d-band shape on the surface reactivity of transition-metal alloys, *Phys Rev B*, 2014, **89**.
55 P. Psarras, R. Anderson, D. A. Gómez-Gualdrón and J. Wilcox, Material Consequences of Hydrogen Dissolution in Palladium Alloys Observed from First Principles, *J Phys Chem C*, 2019, **123**, 22158-22171.
56 V. Pallassana, M. Neurock, L. B. Hansen and J. K. Norskov, First principles analysis of hydrogen chemisorption on Pd-Re alloyed overlayers and alloyed surfaces, *J Chem Phys*, 2000, **112**, 5435-5439.
57 W. J. Xu, D. J. Cheng, M. Niu, X. H. Shao and W. C. Wang, Modification of the adsorption properties of O and OH on Pt-Ni bimetallic surfaces by subsurface alloying, *Electrochim Acta*, 2012, **76**, 440-445.
58 J. R. Kitchin, J. K. Norskov, M. A. Barteau and J. G. Chen, Modification of the surface electronic and chemical properties of Pt(111) by subsurface 3d transition metals, *J Chem Phys*, 2004, **120**, 10240-10246.
59 L. Piccolo, D. Loffreda, F. J. Cadete Santos Aires, C. Deranlot, Y. Jugnet, P. Sautet and J. C. Bertolini, The adsorption of CO on Au(111) at elevated pressures studied by STM, RAIRS and DFT calculations, *Surf Sci*, 2004, **566-568**, 995-1000.
60 B. E. Hayden, K. Kretzschmar and A. M. Bradshaw, An infrared spectroscopic study of CO on Cu(111): The linear, bridging and physisorbed species, *Surf Sci*, 1985, **155**, 553-566.
61 M. J. Kappers and J. H. van der Maas, Correlation between CO frequency and Pt coordination number. A DRIFT study on supported Pt catalysts, *Catal Lett*, 1991, **10**, 365-373.
62 M. Morkel, H. Unterhalt, M. Salmeron, G. Rupprechter and H.-J. Freund, SFG spectroscopy from 10−8 to 1000 mbar: less-ordered CO structures and coadsorption on Pd, *Surf Sci*, 2003, **532-535**, 103-107.
63 J. C. Campuzano and R. G. Greenler, The adsorption sites of CO on Ni(111) as determined by infrared reflection-absorption spectroscopy, *Surf Sci*, 1979, **83**, 301-312.
64 N. Planas, J. E. Mondloch, S. Tussupbayev, J. Borycz, L. Gagliardi, J. T. Hupp, O. K. Farha and C. J. Cramer, Defining the Proton Topology of the Zr6-Based Metal-Organic Framework NU-1000, *J Phys Chem Lett*, 2014, **5**, 3716-3723.
65 H. Li, C. Paolucci, I. Khurana, L. N. Wilcox, F. Goltl, J. D. Albarracin-Caballero, A. J. Shih, F. H. Ribeiro, R. Gounder and W. F. Schneider, Consequences of exchange-site heterogeneity and dynamics on the UV-visible spectrum of Cu-exchanged SSZ-13, *Chem Sci*, 2019, **10**, 2373-2384.
66 P. J. Feibelman, B. Hammer, J. K. Norskov, F. Wagner, M. Scheffler, R. Stumpf, R. Watwe and J. Dumesic, The CO/Pt(111) puzzle, *J Phys Chem B*, 2001, **105**, 4018-4025.
67 G. Blyholder, Molecular Orbital View of Chemisorbed Carbon Monoxide, *J Phys Chem*, 1964, **68**, 2772-&.
68 F. Abild-Pedersen, J. Greeley, F. Studt, J. Rossmeisl, T. R. Munter, P. G. Moses, E. Skulason, T. Bligaard and J. K. Norskov, Scaling properties of adsorption energies for hydrogen-containing molecules on transition-metal surfaces, *Phys Rev Lett*, 2007, **99**, 016105.
69 J. Greeley, Theoretical Heterogeneous Catalysis: Scaling Relationships and Computational Catalyst Design, *Annu Rev Chem Biomol*, 2016, **7**, 605-635.
70 E. M. Fernandez, P. G. Moses, A. Toftelund, H. A. Hansen, J. I. Martinez, F. Abild-Pedersen, J. Kleis, B. Hinnemann, J. Rossmeisl, T. Bligaard and J. K. Norskov, Scaling relationships for adsorption energies on transition metal oxide, sulfide, and nitride surfaces, *Angew Chem Int Ed Engl*, 2008, **47**, 4683-4686.
71 Y. Santiago-Rodriguez, J. A. Herron, M. C. Curet-Arana and M. Mavrikakis, Atomic and molecular adsorption on Au(111), *Surf Sci*, 2014, **627**, 57-69.
72 L. Xu, J. S. Lin, Y. H. Bai and M. Mavrikakis, Atomic and Molecular Adsorption on Cu(111), *Top Catal*, 2018, **61**, 736-750.
73 D. C. Ford, Y. Xu and M. Mavrikakis, Atomic and molecular adsorption on Pt(111), *Surf Sci*, 2005, **587**, 159-174.
74 J. A. Herron, S. Tonelli and M. Mavrikakis, Atomic and molecular adsorption on Pd(111), *Surf Sci*, 2012, **606**, 1670-1679.
75 Y. H. Bai, D. Kirvassilis, L. Xu and M. Mavrikakis, Atomic and molecular adsorption on Ni(111), *Surf Sci*, 2019, **679**, 240-253.
76 T. H. Yu, T. Hofmann, Y. Sha, B. V. Merinov, D. J. Myers, C. Heske and W. A. Goddard, Finding Correlations of the Oxygen Reduction Reaction Activity of Transition Metal Catalysts with Parameters Obtained from Quantum Mechanics, *J Phys Chem C*, 2013, **117**, 26598-26607.
77 Z. N. Xu and J. R. Kitchin, Probing the Coverage Dependence of Site and Adsorbate Configurational Correlations on (111) Surfaces of Late Transition Metals, *J Phys Chem C*, 2014, **118**, 25597-25602.
78 P. Majumdar and J. Greeley, Generalized scaling relationships on transition metals: Influence of adsorbate-coadsorbate interactions, *Phys Rev Mater*, 2018, **2**.
79 S. Back, J. Yoon, N. Tian, W. Zhong, K. Tran and Z. W. Ulissi, Convolutional Neural Network of Atomic Surface Structures To Predict Binding Energies for High-Throughput Screening of Catalysts, *J Phys Chem Lett*, 2019, **10**, 4401-4408.
80 Z. Li, S. Wang, W. S. Chin, L. E. Achenie and H. Xin, High-throughput screening of bimetallic catalysts enabled by machine learning, *J Mater Chem A*, 2017, **5**, 24131-24138.
81 J. Noh, S. Back, J. Kim and Y. Jung, Active learning with non-ab initio input features toward efficient CO2 reduction catalysts, *Chem Sci*, 2018, **9**, 5152-5159.
82 M. Andersen, S. V. Levchenko, M. Scheffler and K. Reuter, Beyond Scaling Relations for the Description of Catalytic Materials, *ACS Catal*, 2019, **9**, 2752-2759.
83 J. H. Friedman, Greedy function approximation: A gradient boosting machine, *Ann Stat*, 2001, **29**, 1189-1232.

TOC

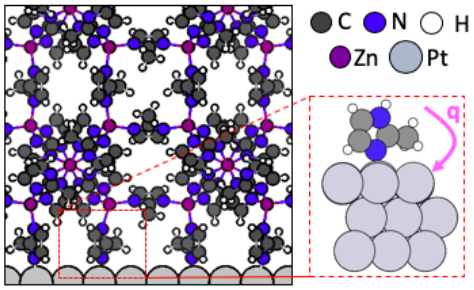

Highlight sentence

Using approximated NP/MOF interface models, DFT was used to investigate MOF-originated electronic effects on encapsulated NPs in NP@MOF hybrid catalysts